

Article

Hybrid Heat Pipe-PCM-Assisted Thermal Management for Lithium-Ion Batteries

Nourouddin Sharifi ^{1,*}, Hamidreza Shabgard ², Christian Millard ³ and Ugochukwu Etufugh ³

¹ Department of Engineering Technology, Tarleton State University, 1333 W. Washington, Stephenville, TX 76402, USA

² School of Aerospace and Mechanical Engineering, University of Oklahoma, 865 Asp Ave., Norman, OK 73019, USA; shabgard@ou.edu

³ Department of Mechanical, Environmental, and Civil Engineering, Tarleton State University, 1333 W. Washington, Stephenville, TX 76402, USA; christian.millard@go.tarleton.edu (C.M.); ugochukwu.etufugh@go.tarleton.edu (U.E.)

* Correspondence: sharifi@tarleton.edu

Abstract: A hybrid cooling method for 18650 lithium-ion batteries has been investigated using both experimental and numerical approaches for electric vehicle applications. The experimental setup includes a heater section, a phase change material (PCM) reservoir, and a cooling section. The heater section simulates battery heat generation with two cylindrical aluminum housings, each sized to match an 18650 battery, two cartridge heaters, and an aluminum heat sink. An airflow channel is incorporated into the cooling section. Heat transfers sequentially from the heaters to aluminum housings, the heat sink, through three copper-water heat pipes (HPs), to/from the PCM, and finally to the cooled air in the airflow channel. This innovative design eliminates direct contact between the PCM and the batteries, unlike recent studies where the PCM has been in direct contact with the batteries. Decoupling the PCM reduces system design complexity while maintaining effective thermal management. Temperature measurements at various locations are analyzed under different heater powers, air velocities, and scenarios with and without PCM. Results show that the experimental design effectively maintains battery temperatures within acceptable limits. For a power input of 16 W, steady-state temperatures are reduced by approximately 14%, 10%, and 4% with PCM compared to without PCM for air velocities of 2 m/s, 3 m/s, and 4 m/s, respectively. A transient three-dimensional numerical model was developed in ANSYS-FLUENT to provide insights into the underlying physics. The phase change was simulated using the enthalpy-porosity approach, with computational results showing reasonable agreement with experimental data.

Keywords: thermal management; battery; heat pipes; PCM; EV



Academic Editor: Mingtao Li

Received: 6 January 2025

Revised: 28 January 2025

Accepted: 6 February 2025

Published: 7 February 2025

Citation: Sharifi, N.; Shabgard, H.; Millard, C.; Etufugh, U. Hybrid Heat Pipe-PCM-Assisted Thermal Management for Lithium-Ion Batteries. *Batteries* **2025**, *11*, 64. <https://doi.org/10.3390/batteries11020064>

Copyright: © 2025 by the authors. Licensee MDPI, Basel, Switzerland. This article is an open access article distributed under the terms and conditions of the Creative Commons Attribution (CC BY) license (<https://creativecommons.org/licenses/by/4.0/>).

1. Introduction

Automakers are creating more electric vehicles (EVs) and accelerating the development of EV technology in response to the growing desire to reduce the carbon footprint of transportation. Despite the growing demand, the broad integration of EVs in the general automotive market continues to be hindered by several challenges. Consumer complaints include the EV's short vehicle lifespan, especially in relation to the battery pack's longevity, and its unreliability for long-distance driving. An EV battery pack's performance is influenced by multiple factors, the primary one being its vulnerability to temperature impacts. Ma et al. [1] reviewed the effects of temperature on lithium-ion batteries.

Typically, the safe temperature range for lithium-ion batteries spans from $-20\text{ }^{\circ}\text{C}$ to $60\text{ }^{\circ}\text{C}$, with the optimal operating range being between $15\text{ }^{\circ}\text{C}$ and $35\text{ }^{\circ}\text{C}$ [1]. Temperatures exceeding the operating limit may cause an irreversible reaction to occur across the lithium-ion battery pack and raise the possibility of thermal runaway. Thermal runaway is characterized by an increase in temperature that releases energy and then causes another increase in temperature [1]. The discharge of thermal energy into the surrounding environment raises the temperature and internal energy of all adjacent batteries. Thermal runaway causes degradation over time and shortens the battery's life. Battery thermal management (BTM), a term for a variety of temperature control techniques, can be used to control this extremely harmful process. Therefore, ongoing developments in effective cooling technologies will increase the overall longevity and safety of the battery packs in electric vehicles. Three primary approaches to battery thermal management have been thoroughly examined by earlier researchers [2–5]: active, passive, and hybrid cooling methods. Passive cooling techniques use mainly heat pipes (HPs) and phase change materials (PCMs), while active cooling techniques use an actively induced flow. The advantages of both active and passive cooling techniques are combined in the hybrid approach. The ability of PCMs to absorb significant amounts of latent heat within a narrow temperature range [6] makes them appealing for passive BTM. Nevertheless, a drawback of most PCMs is their limited heat conductivity, which restricts their range of use.

One approach to improving the heat transfer rate of PCMs is by incorporating HPs. Through the evaporation and condensation of their working fluid, HPs serve as efficient thermal devices that can passively transfer substantial amounts of heat across small cross-sectional areas [7]. The background and history of research on the benefits of integrating HPs with fins and PCM to enhance heat transfer have been investigated extensively by previous researchers [8–11].

In recent advancements, researchers have explored thermal management systems for 18650 lithium-ion batteries utilizing hybrid HP–PCM configurations. These studies commonly consider designs where the PCM and batteries are housed within an enclosure forming a battery pack, with PCM in direct contact with the batteries. Heat pipes are integrated into the PCM such that the evaporator section is positioned within the battery pack while the condenser section is air-cooled. To enhance cooling performance, the evaporator and condenser sections of the HPs are often equipped with fins. Overall, these studies demonstrate that hybrid HP–PCM systems offer notable advantages in reducing maximum battery temperatures and improving temperature uniformity. Below is a summary of recent developments in this field with similar design configurations as explained above, emphasizing their findings and distinguishing features.

Gao et al. [12] conducted a numerical evaluation of a hybrid HP–PCM system where HPs were in direct contact with both the batteries and the PCM. Their results showed a reduction in maximum temperatures by 25.7%, 23.3%, and 34.9% for discharge rates of 2C, 3C, and 4C, respectively, compared to PCM-only systems. Similarly, Sutheesh et al. [13] numerically explored hybrid cooling systems incorporating HPs with nano-enhanced PCM. Their study investigated different cell arrangements, revealing that a horizontal cell arrangement performed better by maintaining the battery pack within the desired temperature range for 65% of the discharge process at a 3C rate. Sharma et al. [14] advanced hybrid systems by integrating fins with flat-plate HPs and PCM through both numerical and experimental analyses. They studied various fin configurations, identifying an optimized design that reduced peak battery temperatures by $2.95\text{ }^{\circ}\text{C}$ and maintained surface temperatures below $60\text{ }^{\circ}\text{C}$. Experimental validation confirmed the improved thermal performance during charge-discharge cycles, emphasizing the importance of fin optimization in system design.

Similar studies were conducted by Tang et al. [15], with the exception being that they used copper foam-PCM composites. Abbas et al. [16] also investigated hybrid HP-PCM systems and found better battery temperature uniformity when HPs were attached to the batteries compared to when they were not attached.

This study proposes a configuration for a HP-fin-assisted, PCM-based hybrid BTM system designed for 18650-type lithium-ion battery modules. The primary innovation of this work, as compared to the existing literature outlined in the introduction section, lies in the strategic placement of the PCM. Unlike previous designs where the PCM is in direct contact with the batteries, the current configuration decouples the PCM from the battery pack and positions it between the batteries and the air-cooled section. This design offers several practical advantages. By decoupling the PCM, the system removes the PCM size constraints typically imposed by the battery pack dimensions, allowing for greater design flexibility. Moreover, this arrangement simplifies battery replacement, as the PCM is not integrated within the battery pack. As a result, the overall system design is streamlined, and complexity is reduced.

Furthermore, to the authors' knowledge, no prior studies have developed numerical simulations in ANSYS-FLUENT that fully solve the governing equations of HPs, coupled with conjugate heat transfer in the PCM and fins. This aspect strengthens the uniqueness of the present work. In previous studies involving HP-fin-PCM systems, researchers have often treated HPs as materials with high effective thermal conductivity or modeled them as thermal resistance networks, rather than solving their full governing equations. The numerical model developed in this study represents a significant advancement by thoroughly capturing the physical processes within the HPs, PCM, and fins.

2. Experimental Design

The explanation of the experimental setup is divided into four subsections: (i) the heating section, (ii) the PCM reservoir, (iii) the 3D-printed supports and insulation, and (iv) the air-cooling section, each of which is described in detail below.

2.1. Heating Section

The experiments in this study required numerous battery charging and discharging cycles, which increased the risk of thermal runaway or potential battery explosion. To avoid the risk of battery explosion and perform the experiment safely in the lab environment, a combination of cartridge heaters and aluminum housings were used to mimic the heat generated by the batteries.

Figure 1a shows the side view of the setup, detailing the various sections, components, dimensions, and thermocouple locations. The heating section was composed of two aluminum housings (AL 6061), each with inner and outer diameters of about 8 mm and 18 mm, and a length of 65 mm. The aluminum housings had the same exterior dimensions as 18650 lithium-ion batteries. Two cartridge heaters (tatoko, 12 V, 100 W, 8 mm diameter and 100 mm length) were inserted concentrically into the aluminum housings. Thermal paste (arctic silver 5, $k \approx 8.7 \text{ W/m}\cdot\text{K}$) was applied to fill the gap between the heaters and the aluminum housings, aiming to reduce thermal contact resistance. The heaters were powered with a DC power supply (B&K Precision 1671A, Yorba Linda, California, Address: 22820 Savi Ranch Pkwy, Yorba Linda, CA 92887, USA).

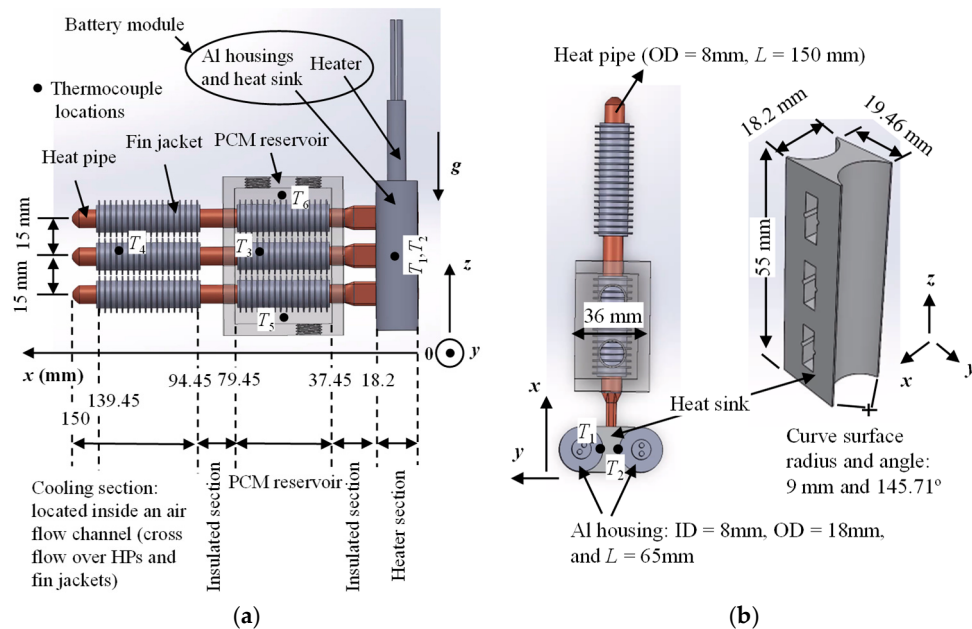


Figure 1. Schematic view of the setup illustrating its components, dimensions, and thermocouple locations: (a) Side view; (b) Top view.

Three cylindrical copper-water HPs (Advanced Thermal Solutions Inc. (Norwood airport business park, Address: 89 Access Rd STE 27, Norwood, MA 02062, USA): ATS-HP-6L150S71W-129, 8 mm diameter and 150 mm length) were utilized in this setup to transfer heat from the heating section to the PCM and cooling section. To increase compactness on the battery side, a portion of the cylindrical HPs were carefully flattened using a bench vise. Hence, the HPs were referred to as partially flattened cylindrical HPs. The flat portion of each HP had an approximate length of 27.2 mm and measured about 4.2 mm in the y -direction and 10.5 mm in the z -direction. A heat sink was designed to connect the flat portion of the HPs to the aluminum housings, with further details provided later. The heaters, aluminum housings, heat sink, and HPs were all in direct contact. Thermal paste was used at the interface of the aluminum housing–heat sink and the HPs–heat sink. The combination of the heaters, the heat sink, and the Al housings is called the battery module hereafter.

The thermocouples T_1 and T_2 were installed at the mid-height of the aluminum housing–heat sink interface on each side of the heat sink, where they were in contact with the two aluminum housings. The readings of these two thermocouples were very close due to the setup's symmetry with respect to the HP's mid x – z plane. Considering that the temperature difference between T_1 and T_2 was within $0.5\text{ }^{\circ}\text{C}$ at any instant, the temperature T_B , defined as the instantaneous average of T_1 and T_2 , $T_B = (T_1 + T_2)/2$, was reported as the battery temperature in all experiments. It should be noted that T_B is not a physical thermocouple installed on the setup, but rather an average of two thermocouples. The thermocouple T_3 recorded the middle HP–fin jacket interface at $x = 69.45$ mm. The purpose of thermocouple T_3 was to capture more detailed phase change phenomena and their impacts in the case with PCM, compared to the scenario without PCM. To securely position this thermocouple, small longitudinal grooves were created on the interior surface of the fin jacket, providing space to insert the thermocouple at the HP–fin jacket interface. Thermocouples T_5 and T_6 were installed within the PCM about 2 mm from the mid-bottom interior surface of the PCM reservoir and the mid-top surface of the PCM, respectively, and were used to record the PCM temperatures to estimate the melting process duration. They were removed for experiments without the PCM.

Figure 1b shows the top view of the setup, including the detailed dimensions of the heat sink. To ensure efficient heat transfer between the aluminum housings and the HPs, a heat sink (AL 6061) was designed and manufactured using a desktop CNC machine. The heat sink has a length of 55 mm and is in contact with the mid 65 mm length of the exterior surface of the aluminum housings. The top and bottom of the exterior surface of the aluminum housings (each 5 mm) are not in contact with the heat sink. These 5 mm lengths will allow extra space between the batteries' bus bar and the batteries' top and bottom caps, mimicking a real battery pack. The heat sink includes three slots, each with an approximate dimension of 11 mm by 4.2 mm. Each partially flattened cylindrical HP was inserted into the slots. Grooves (~0.6 mm in radius) were machined in each slot of the heat sink to accommodate thermocouples.

2.2. PCM Reservoir

In this study, 1-Tetradecane (99% pure C₁₄H₃₀O) was selected as the PCM, with a melting temperature of approximately 38 °C [17]. While various PCMs with different melting temperatures have been used in the literature, Jiang et al. [18] reported that PCMs with melting temperatures lower than 45 °C are more effective for heat dissipation when the maximum allowable battery temperature is below 50 °C. Since the maximum allowable battery temperature in this study was below 50 °C, a PCM with a melting temperature approximately 5–7 °C lower than 45 °C, such as 1-Tetradecane, was chosen. Moreover, this PCM is safe for use up to 100 °C, and is readily available.

A 3D-printed enclosure (PCM reservoir) was designed and created to hold a measured amount of PCM (see Figure 1a,b). The interior dimensions of the enclosure are 42 mm in the *x*-direction, 26 mm in the *y*-direction, and 59 mm in the *z*-direction, and the wall thickness is about 5 mm. The reservoir has six holes in the *x*-direction, each with a diameter of about 8 mm. It was made to properly house the HPs, as well as mate well with the battery module support surface. The holes for the HPs are about 15 mm apart from center to center. There are additional threaded thru holes on the top and bottom for filling and draining the PCM.

To enhance the heat transfer rate within the PCM, three aluminum fin jackets (AL 6061) were designed and machined using a manual lathe. The annular fin jackets in the PCM reservoir each have a length of 40 mm, an inner diameter of about 8 mm, a wall thickness of about 1.5 mm, an approximate fin thickness of 0.5 mm, a fin length of 2 mm, and a fin spacing of 2.5 mm.

The PCM reservoir was open on the side wall, and a lid was used to close the opening. This opening facilitated the inserting of the fin jackets and the installation of thermocouples during assembly. Caps were used to close the top and bottom openings of the PCM reservoir. An aquarium silicone sealant was then used to prevent any PCM leakage from the PCM reservoir.

2.3. 3D-Printed Supports and Insulation

Figure 2 presents an isometric view of the experimental setup, both with and without the insulation box. As shown in Figure 2a, PLA plastic 3D-printed parts called battery module supports were created to hold and support the aluminum housings, heaters, heat sink, and HPs, keeping these components in place. The battery module support was made to be screwed together at four threaded thru holes at the top and bottom. It also accounted for the thermocouples that were attached during experimentation. To achieve this, 2 mm semi-circular slots were incorporated into the design. Furthermore, 3D-printed heater sleeves were also created to insulate and support the heaters. A 3D-printed base plate was created to secure the components in place and allow for better leveling of the setup. As illustrated in Figure 2b, a double-pane (~5 mm air gap) insulation box was also 3D-printed

to enclose the setup for insulation purposes. The setup is geometrically symmetric with respect to its (*x-z*) mid-plane.

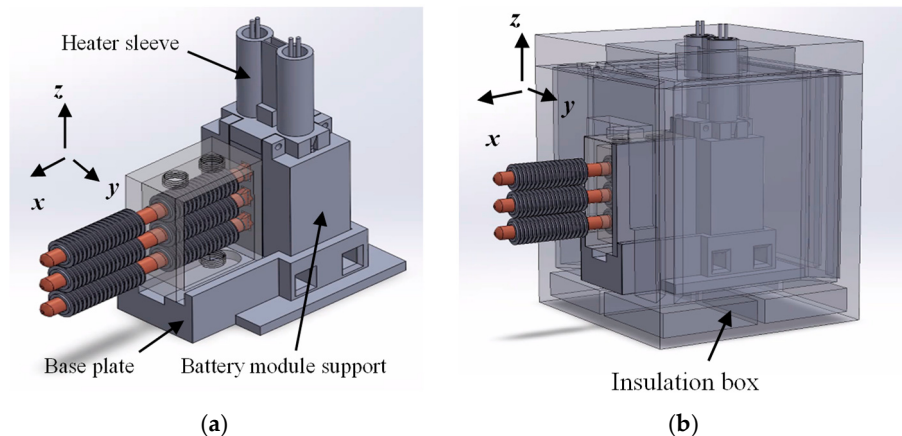


Figure 2. Isometric view of the experimental setup showing: (a) Without insulation box, including the base plate, battery module support, and heater sleeve; (b) With all components and the insulation box (the insulation box is transparent in this figure for clarity).

To enhance thermal insulation, a 10 mm-thick aerogel insulation pad (MARSTEP-NASA Tech, $k \approx 0.025 \text{ W/mK}$ [19]) was placed between the 3D-printed battery module support and the PCM reservoir, between the PCM reservoir and the flow channel wall, and around the battery module supports and heaters within the insulation box.

2.4. Cooling Section

Figure 3 illustrates a schematic of the flow channel and the setup. As shown in Figure 3a, an air flow channel was constructed to provide a forced convection thermal boundary condition on the condenser section of the HPs (portion of the HPs within the flow channel). The internal measurements of the flow channel are approximately 1 m in length (*y*-direction), 160 mm in width (*x*-direction), and 180 mm in height (*z*-direction). The centerline of the setup, along the *x*-direction, is approximately 620 mm from the inlet of the channel. The flow channel walls were constructed from a 5 mm thick acrylic sheet. A fan (VEVOR inline duct fan, 4-Inch 200 CFM with variable speed controller, Model: BT-FL14A, 120 VAC/60 Hz 31 W) was used to create a steady flow of air through the channel by creating suction at the outlet. A bank of 100 mm long, thin-walled, 5 mm-diameter plastic tubes (drinking straws) was used as a honeycomb-type flow straightener. The air speed was measured using a hot wire anemometer (Koselig Instruments, Model: KI-10001, ASIN: B08QRC756F, 0.1–25 m/s, accuracy: 1% full range, resolution: 0.01).

Fin jackets were also employed to enhance the heat transfer rate from the HPs to the cooling air. The fin jackets have the same dimensions as those used within the PCM reservoir, with the exception that their length is about 45 mm. Thermal paste was used between the fin jackets and the HPs.

The component dimensions in the experimental setup were estimated based on the minimum heat transfer area required to achieve a cooling capacity of 8W per battery, within a fan speed range of 0 to 4 m/s. The 8W power corresponds to a high discharge rate of 5C for an individual battery [20]. Specifically, the number of HPs, their dimensions, and the fin dimensions were calculated by determining the necessary heat transfer area through convective heat transfer analysis. The fin lengths were constrained by the heat sink length, the number of HPs, and their diameters. The dimensions of the aluminum housings and heat sink were constrained by the size of the 18650 lithium-ion battery. The PCM reservoir dimensions were selected based on the minimum volume of PCM required

to encapsulate all three HPs with fin jackets within the reservoir. Additionally, sufficient space was allocated to facilitate the installation of the fin jackets on the HPs within the PCM reservoir, as well as the necessary placement of thermocouples.

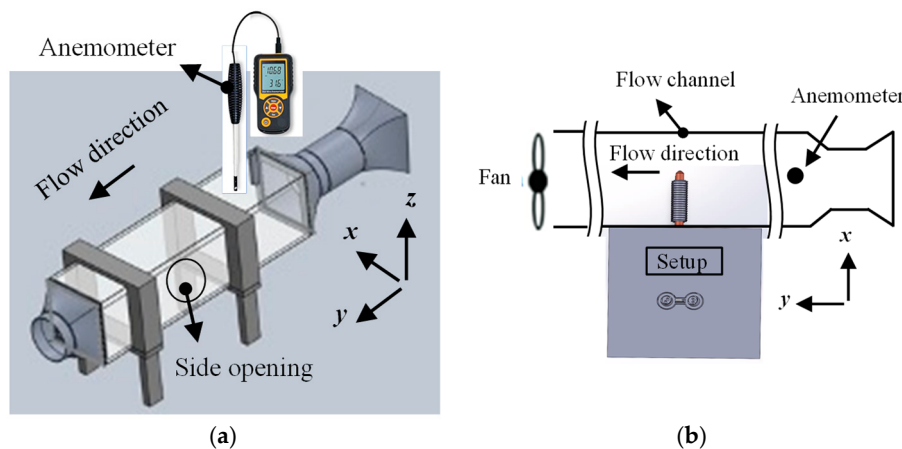


Figure 3. Isometric of the experimental setup within its insulation box with flow channel: (a) Isometric view showing the flow channel for the air-cooling section of the setup; (b) Top view showing the air-cooling section of the setup positioned with the flow channel through its side opening, with air flowing crosswise over the HPs and fin jackets.

Temperatures at specific locations were recorded with Teflon-coated, 254- μm -diameter chrome-alumel (K-type) thermocouples. The calibration of the thermocouples was verified using the boiling and freezing points of distilled water. The thermocouples were positioned with an accuracy of approximately ± 1 mm. Aluminum tape was used to secure the thermocouples in place. Thermocouple voltage readings were recorded at 1 s intervals using four OMEGA TC-08 USB thermocouple data acquisition modules, managed through Picolog 6 software. The measurement error for each point was ± 0.5 °C, attributed to system uncertainties involving the data acquisition device and thermocouples. Additionally, the uncertainty in the heating power measurement was less than 5%. Table 1 displays the thermophysical properties of 1-Tedadecanol, the HP, and the fin jacket.

Table 1. Thermophysical properties of HP and fin jacket.

	PCM	HP Working Fluid	HP Wall (≈ 0.5 mm) and Wick (≈ 1 mm)	Fin Jacket
Material	1-Tedadecanol [10]	Water [10]	Copper [8]	Aluminum 6061 [21]
Density, ρ (kg/m ³)	823 (liquid)	996.6 (liquid)	8933	2700
Thermal conductivity, k (W/m K)	0.481 (solid) 0.22 (liquid)	0.6132 (liquid) 0.01932 (vapor)	401	167
Specific heat, c_p (J/kg K)	2407	4181 (liquid) 1882 (vapor)	385	896
Viscosity, μ (Pa.s)	0.0064	8614×10^{-7} (liquid) 91.74×10^{-7} (vapor)		
Latent heat of fusion, $h_{\text{f}} (\text{kJ/kg})$	235.41			
Latent heat of vaporization, h_{fg} (kJ/kg)		2434.9		
Melting temperature, T_m (°C)	38			

Table 1. Cont.

	PCM	HP Working Fluid	HP Wall (≈ 0.5 mm) and Wick (≈ 1 mm)	Fin Jacket
Thermal expansion coefficient β (1/K)	0.00084			
Vapor pressure, P_{sat} (Pa)		4352		

3. Experimental Procedure

Two cooling scenarios were investigated in this study: (i) without the PCM, and (ii) with the PCM, each at various input powers and air velocities. For the case without PCM, the aerogel insulation pad was cut into small pieces and inserted into the PCM reservoir to insulate the portion of the HPs within the PCM reservoir. For the PCM experiments, testing commenced with the PCM in a solid state and at a uniform temperature. Precautions were taken to ensure the PCM was void-free. To do so, the PCM was slowly melted in a beaker over a plate heater. The warm, molten PCM was carefully poured into the PCM reservoir (refer to the setup in Figure 2a with the base plate), forming an initial PCM layer approximately 5 mm thick. The test cell was then allowed to cool naturally in ambient air ($T_{\text{air}} < T_m$) to solidify the PCM. Once this layer was hardened, the pouring and solidifying process was repeated until the enclosure was filled with solid PCM. To account for the expansion of the PCM upon melting, a 3 mm air gap was maintained in the enclosure.

The setup was left to stabilize at room temperature (~21.5 °C) for approximately 24 h. Afterwards, it was insulated with aerogel pads and placed inside the insulation box (see Figure 2b). The insulation box with the setup was connected to the flow channel by placing the cooling section of the HPs into the air channel through its side opening, as shown in Figure 3b. Four heater power levels were tested, with each heater individually powered at 4 W, 6 W, 8 W, and 10 W, yielding total powers of 8 W, 12 W, 16 W, and 20 W per experiment. The fan speed was adjusted to achieve air velocities of 0 m/s, 2 m/s, 3 m/s, and 4 m/s, corresponding to air flow rates of 0, 0.058 m³/s, 0.087 m³/s, and 0.116 m³/s, respectively, through a flow channel with an interior cross-sectional area of about 0.029 m². The different combinations of heating power and air speed produced temperatures comparable to the temperatures within an 18650 lithium-ion battery, specifically for relatively higher discharge rates, i.e., from 2 C to 4 C (see Figure 7 of reference [5] and Figure 17a of reference [20]). The setup was assumed to be thermally symmetric with respect to the HPs mid x - z plane.

4. Physical Model and Mathematical Formulation

A three-dimensional numerical model was developed using ANSYS-FLUENT 2023 software to explore the underlying physics of the problem, offering insights that could not be obtained solely from experimental studies. This model also facilitated optimization studies of the setup. The numerical approach employed the transient enthalpy-porosity technique. The conservation equations for mass, energy, and momentum were fully solved across the entire computational domain. The heat transfer phenomena were driven by transient and coupled effects, including: (i) conduction through solid walls (such as Al housings, heat sinks, fin jackets, and HPs' walls and wicks), (ii) vaporization, condensation, and incompressible flow of the HPs' working fluid, (iii) natural convection occurring within the PCM during phase transitions, and (iv) forced convection in the cooling section of the experimental setup. A User-Defined Function (UDF) was created and incorporated into the FLUENT software to improve the detailed modeling of the HPs. To reduce the complexity of the numerical simulation, it was divided into two different parts. In the first part, air flow over the HPs and fin jackets within the flow channel was simulated to determine the

corresponding average convective heat transfer coefficients. The computational domain for this part is depicted in Figure 4a. The interior dimensions of the computational domain and the positioning of the HPs relative to the airflow channel align with the details provided in the cooling section of the experimental design. Due to the model's symmetry along the $x-y$ plane at the center of the middle HP in this configuration, only the top half of the physical domain was considered for simulation. In the second part, the setup comprising the heat sink, HPs, PCM, and fin jackets was simulated. The computational domain for this part is illustrated in Figure 4b, shown in two isometric views of the same domain. Due to the symmetry of the model along the $x-z$ plane, only half of the physical domain is represented. The average convective heat transfer coefficients obtained from the first part, with the computational domain shown in Figure 4a, were uniformly applied as convective thermal boundary conditions on the exterior surfaces of the HPs and fin jackets exposed to the air.

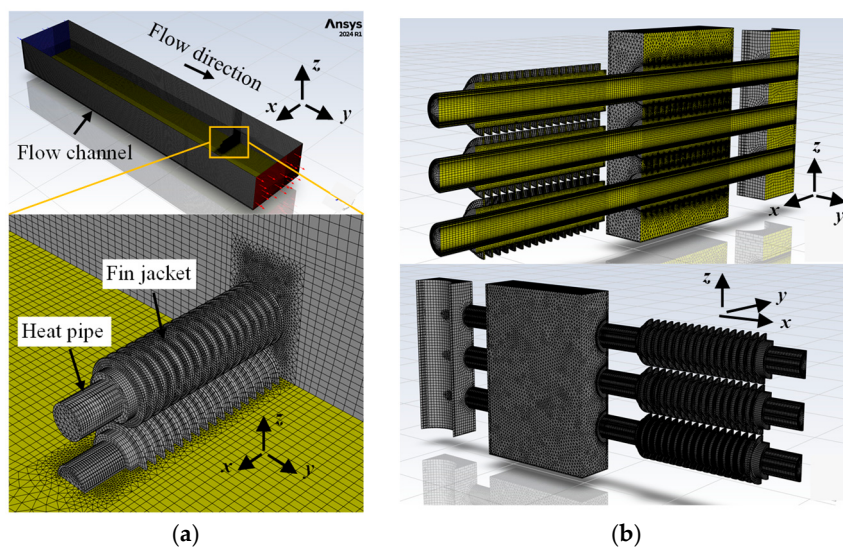


Figure 4. Computational domains: (a) Air-cooling section of the setup within the flow channel; (b) Half of the HP-fin-PCM physical domain.

The model was based on several assumptions: all thermophysical properties were considered constant, except for the vapor phase of the HPs' working fluid, which was treated as an ideal gas, resulting in a density that varies with temperature and pressure. The solid PCM was assumed to be pure, and the molten PCM was assumed to have the same density as the solid PCM. Natural convection in the molten PCM was modeled using the Boussinesq approximation. The phase change process was represented through the enthalpy-porosity method [22]. Thermal radiation was considered negligible due to the relatively low temperatures involved. The vapor phase of the HPs' working fluid was modeled as undergoing three-dimensional laminar incompressible flow, with the wick fully saturated. At the wick interface, both the vapor and liquid phases of the working fluid were in a saturated state. It was assumed that the porous wick generated sufficient capillary pressure to drive the liquid flow through the wick under the operating conditions considered in this study.

Multiple physical boundaries divided the different materials, material phases, and components within the conjugate system. Thermal contact resistances were ignored. The computational domain depicted in Figure 4b is governed by the following boundary and initial conditions. Symmetry conditions were applied along the mid $x-z$ plane of the setup. A constant, uniform heat flux was imposed on the external surface of the heat sink in contact with the aluminum housing. The remaining external boundaries were set as adiabatic

and impermeable, with no-slip conditions applied. A convective heat transfer condition was applied to the outer surfaces of the HPs and fin jackets within the flow channel. The initial temperature of the entire domain was initially set to the laboratory temperature of approximately 21.5 °C.

Given the aforementioned assumptions, the governing equations for the HPs, PCM, and solid walls are expressed as follows:

4.1. Descriptive Equations for the Heat Pipe

The vapor flow within the HP is described by the following Equations [23]:

$$\frac{\partial}{\partial t}(\rho_v) + \nabla \cdot (\rho_v \mathbf{V}) = 0 \quad (1)$$

$$\frac{\partial}{\partial t}(\rho_v \mathbf{V}) + \nabla \cdot (\rho_v \mathbf{V} \mathbf{V}) = -\nabla P + \mu_v \nabla \cdot (\nabla \mathbf{V} - \nabla \mathbf{V}^T) \quad (2)$$

$$\frac{\partial}{\partial t}(\rho_v \mathbf{V}) + \nabla \cdot (\rho_v \mathbf{V} \mathbf{V}) = -\nabla P + \mu_v \nabla \cdot (\nabla \mathbf{V} - \nabla \mathbf{V}^T) \quad (3)$$

The ideal gas law is used to determine the vapor density as a function of its pressure and temperature.

$$\rho = \frac{P}{R_g T} \quad (4)$$

where R_g is the gas constant and is calculated by dividing the universal gas by atomic mass of the vapor. The compressibility factor was calculated to be approximately 0.99 and remained nearly constant under the operating conditions of this study, confirming the validity of the ideal gas assumption for water vapor within the HP.

The heat flux at the wick-vapor interface was used to calculate the evaporation/condensation rate at the interface. This was accomplished by using the following equation:

$$q''_{\text{interface}} = (\dot{m}'' h_{fg})_{\text{interface}} = (\rho_v v_v h_{fg})_{\text{interface}} \quad (5)$$

Equation (5) was also used to calculate the vapor velocity at the interface.

The local wick-vapor interfacial temperatures were obtained from the local vapor pressures adjacent to the interface. During evaporation, the temperature of the vapor is equal to the saturation temperature corresponding to the local pressure. Here, the Antoine equation was used to establish the relationship between the saturation temperature and pressure [24].

$$T_{\text{sat}} = 39.72 \text{ K} + \frac{1730.63}{8.07 - \log_{10} P} \quad (6)$$

where T_{sat} is in K, and P is the absolute pressure of the vapor in the computational cell adjacent to the interfacial node in mmhg (1 Pa = 0.0075 mmhg). The interfacial vapor velocity and saturation temperature, obtained from Equation (5) and Equation (6), respectively, were implemented by a UDF written in C++ and integrated into the ANSYS-FLUENT solver.

In accordance with Cao and Faghri [25], it was assumed that the porous wick of the HP was fully saturated with liquid, and liquid flow within the wick was neglected. The heat conduction equation for all solid materials, including the aluminum housings, heat sink, HP walls and wicks, and fin jackets in the setup, is governed by

$$\frac{\partial(\rho c_p)_w}{\partial t} = k_w \nabla^2 T \quad (7)$$

4.2. Descriptive Equations for the PCM

The enthalpy-porosity method, implemented in ANSYS-Fluent, was used to model the solid-liquid phase change of the PCM. The continuity, momentum, and energy conservation equations for the PCM are formulated as follows [22]:

$$\frac{\partial}{\partial t}(\rho) + \nabla \cdot (\rho \mathbf{V}) = 0 \quad (8)$$

$$\frac{\partial}{\partial t}(\rho \mathbf{V}) + \nabla \cdot (\rho \mathbf{V} \mathbf{V}) = -\nabla P + \mu_v \nabla^2 \mathbf{V} + \rho g [\beta(T - T_m) - 1] + S_m \quad (9)$$

$$\frac{\partial}{\partial t}(\rho H) + \nabla \cdot (\rho \mathbf{V} H) = k \nabla^2 T \quad (10)$$

The specific enthalpy H , as used in Equation (10), is defined as the sum of the sensible enthalpy (h) and the latent enthalpy (ΔH) [22]:

$$H = h + \Delta H = h_{\text{ref}} + \int_{T_{\text{ref}}}^T C_p dT + \lambda(T) L_f \quad (11)$$

Here, the enthalpy h_{ref} is calculated at reference temperature T_{ref} , where L_f represents the latent heat of fusion, and T_{ref} is set to 21.5 °C. The liquid fraction $\lambda(T)$, by definition, is temperature-dependent and is mathematically expressed as follows [22]:

$$\lambda(T) = \frac{\Delta H}{L_f} = \frac{T - T_s}{T_l - T_s} = \begin{cases} 0 & \text{if } T < (T_m - \Delta T) \\ \frac{T - T_m + \Delta T}{2\Delta T} & \text{if } (T_m - \Delta T) \leq T \leq (T_m + \Delta T) \\ 1 & \text{if } T > (T_m + \Delta T) \end{cases} \quad (12)$$

From Equation (12), the liquid fraction is zero for the solid PCM and equal to 1 for the liquid PCM. The source term in the momentum equation, S_m in Equation (9), accounts for the flow through porous media in the mushy zone, where the phase transition takes place. This is modeled using a modified version of the Carman–Kozeny equation [22]. S_m can be expressed as:

$$S_m = A \mathbf{V} = -\frac{A_{\text{mush}}(1 - \lambda)^2}{\lambda^3 + \varepsilon} \mathbf{V} \quad (13)$$

As outlined in [26], the purpose of the source term $A \mathbf{V}$ in Equation (13) is to suppress flow within the mushy zone and gradually halt it as the PCM approaches complete solidification. Specifically, the value of A is zero when the PCM is fully in the liquid phase ($\lambda = 1$), while it becomes significantly large when the PCM is fully solidified ($\lambda = 0$). This source term in the momentum equation is active only during the phase transition, specifically within the melting regime. Further details on the importance and implementation of this source term can be found in the literature [22]. Consequently, the value of A_{mush} must be sufficiently high, typically $\geq 10^3 \text{ kg}/(\text{m}^3 \cdot \text{s})$, to effectively inhibit flow in the solid phase of the PCM. Larger values of A_{mush} result in a relatively slow-moving melting front, as indicated by the reduced velocity magnitudes within the PCM, in accordance with Equation (13). Conversely, smaller values of A_{mush} may lead to an overestimation of the melting rate. Additionally, the value of A_{mush} is influenced by the temperature range of the phase transition, as noted in [22]. In this study, the default value of A_{mush} value of 100,000 provided a satisfactory agreement with the experimental data. A small constant ε ($= 0.001$) was employed to maintain the validity of Equation (13) when $\lambda \rightarrow 0$.

5. Results and Discussion

Following the detailed explanation of the experimental design, procedure, and the underlying physical model, the results obtained from both experimental and numerical

analyses are now presented and discussed. This section is divided into two subsections: experimental results, where the findings from the physical tests are analyzed, and numerical results, which focuses on the computational simulations. These results are compared and contrasted to assess the performance of the hybrid HP–PCM system, providing a comprehensive understanding of its thermal management capabilities.

5.1. Experimental Results

The following subsections present the experimental results for two scenarios: with and without PCM, along with the related discussions. In these experiments, the total power associated with two cartridge heaters was denoted as P_t . The power of each battery was $P_B = P_t/2$. The total power of P_t was transferred from the three HPs toward the PCM (if the PCM is used) and then to the cooling air in flow channel. The initial temperature for all experiments was approximately 21.5 °C, with a variation of approximately ±0.5 °C. Each experiment was performed twice to evaluate the repeatability of the results and to analyze the influence of initial temperature variations on the outcomes. Slight discrepancies were noted between the two sets of results, with instantaneous temperature measurements differing by no more than 1 °C. The experimental results presented in this study represent the averaged values obtained from both experiments.

5.1.1. Without PCM

Figure 5 shows the battery temperature for different total powers and air velocities when no PCM was used (referred to as W/O PCM in figures). Heat pipes were cooled by natural convection when V_{air} was zero, and were cooled by forced convection when V_{air} was non-zero. As expected, the battery temperature was increased (decreased) by increasing the total input power (air velocity). Temperatures reached a steady-state condition within approximately 2 h of operation when $V_{air} \geq 2$ m/s. Steady-state conditions are defined when temperature variations over 5 min are less than 1 °C. For natural convection cooling experiments, the testing was halted once the battery temperature (T_B) reached 80 °C. This precaution was taken to prevent potential thermocouple failure and ensure that temperatures remained within the calibration range of 0 °C to 100 °C. As illustrated in Figure 5, forced convection airflow exerted a substantial influence on reducing battery temperatures across all total power levels. The impacts of air velocities were relatively more significant at higher power.

The experiment deliberately included various power levels and air velocities, irrespective of whether the battery temperature exceeded its safe operational range (below 50 °C). This approach ensured sufficient data to investigate: (i) the correlation between air velocity and battery temperature at each power level within the designed setup, (ii) battery temperature under unexpected conditions such as fan malfunction, and (iii) the identification of combinations of power levels and air velocities that maintained safe battery temperatures for the designed setup.

Inspection of Figure 5 shows that the air velocity had an approximately linear impact on the battery temperatures at a fixed power. Furthermore, it is observed that battery temperatures remained within the safe operational range (below 50 °C) throughout the duration of applied power when the total power levels were below 12 W (corresponding to a battery discharge rate of approximately 4-C [20]) or when air velocities exceeded 4 m/s. However, for other combinations of power levels and air velocities, the duration of input power was constrained to the period before the battery temperature reached 50 °C. For instance, at an air velocity of 2 m/s, the permissible duration of input power was limited to approximately 39 min, 14 min, and 10 min for input powers of 12 W, 16 W, and 20 W, respectively. These durations exhibit an approximate linear correlation

with the input power levels. To ensure the battery temperature remained under 50 °C for the entire duration of application of the above power levels, it was necessary to increase the air velocity to a minimum of 3 m/s (50% increment), 4 m/s (100% increment), and 6 m/s (200% increment). These data suggest an approximate linear relationship between the input power and the required minimum velocity increment. Consequently, this observation supports a practical recommendation for designs utilizing forced convection cooling, emphasizing the necessity of smart fan operation to dynamically control the fan speed based on temperature feedback from the battery. Such an investigation was performed by Zhuang et al. [27] in a battery pack to determine the optimal duration of air circulation for effective cooling and to implement an adaptive cooling strategy that adjusts the cooling intensity based on fluctuations in heat dissipation and energy consumption.

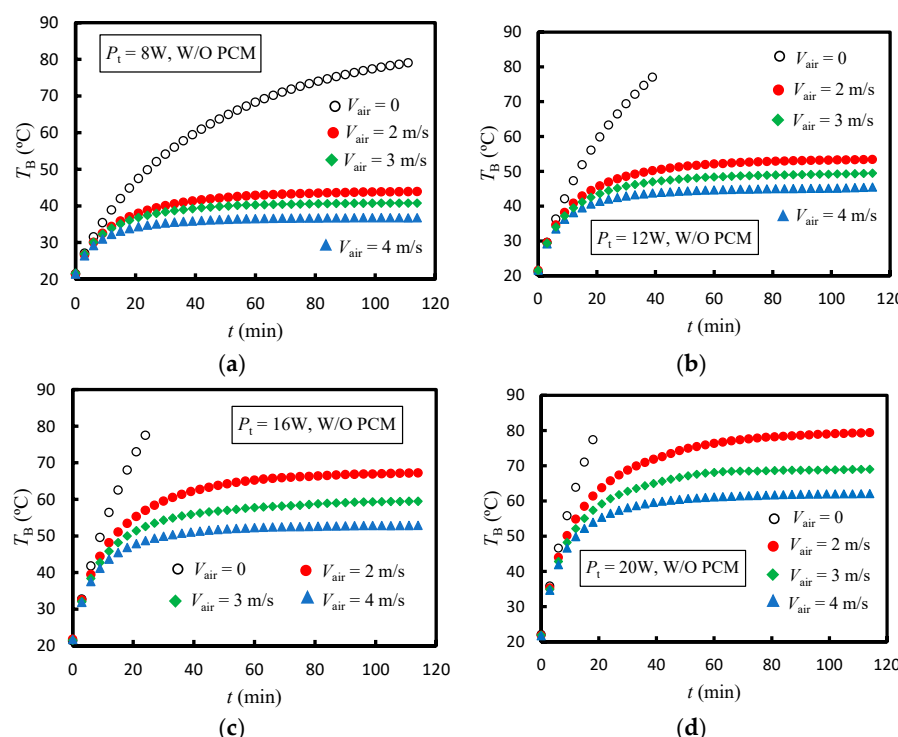


Figure 5. Battery temperature for different total powers and air velocities (without PCM): (a) 8 W; (b) 12 W; (c) 16 W; and (d) 20 W.

5.1.2. With PCM

Figure 6 illustrates the measured temperatures primarily for the “with PCM” scenario at a total power of 16 W and varying air velocities. For comparison, some results from the “without PCM” scenario are also included to highlight the thermal performance improvement achieved with PCM. The 16W total input power selected in this study (equivalent to 8W per individual battery) corresponds to a relatively high discharge rate of 5C [20]. The positions of thermocouples T_3 , T_5 , and T_6 , as well as the definition of T_B derived from T_1 and T_2 , are detailed earlier in the experimental design section. The melting temperature of the PCM ($T_m \approx 38^\circ\text{C}$) is indicated by a solid dashed line.

As shown in Figure 6, the battery temperature (T_B) in the configuration with PCM was significantly lower than in the configuration without PCM. This reduction is attributed to the PCM’s capacity to absorb substantial heat as latent heat during its melting process. The impact of the PCM was more pronounced for relatively lower air velocities because more heat was transferred into the PCM rather than air. For 16 W total power, the battery temperatures (T_B) at $t \approx 110$ min were reduced by about 14%, 10%, and 4% when using the PCM compared to the case without the PCM for air velocities of 2 m/s, 3 m/s, and

4 m/s, respectively. The battery temperature was around or less than 50 °C specifically for cooling air velocities of 3 m/s and 4 m/s. This suggests that, for this setup, air velocities below 3 m/s are not recommended when the total input power is 16 W, unless a smart fan operation increases the fan speed once the battery temperature reaches 50 °C, as discussed in relation to Figure 5.

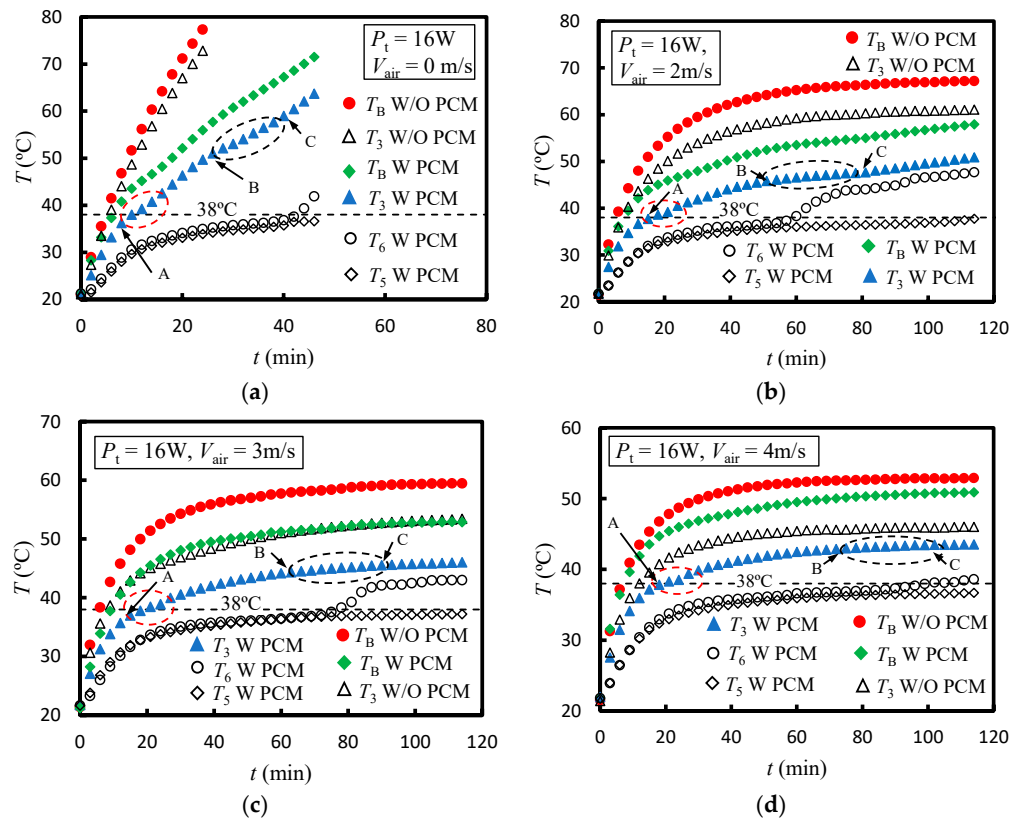


Figure 6. Local temperature histories for a total power of 16W and different air velocities with and without the PCM: (a) 0 m/s; (b) 2 m/s; (c) 3 m/s; and (d) 4 m/s.

A comparison between the time required for T_6 and T_5 to reach 38 °C reveals that the melting process predominantly advanced towards the upper region of the PCM reservoir rather than the lower region. This is because, as melting progressed outward from each fin jacket in the PCM reservoir, the warm molten PCM tended to accumulate towards the top portion of the reservoir.

A comparative analysis between T_3 with and without PCM further emphasized the effect of the PCM's latent heat in absorbing thermal energy from the HPs within the PCM reservoir. For each tested air velocity, T_3 (with PCM) exhibited significantly lower temperatures compared to T_3 (without PCM). The difference between T_3 (with PCM) and T_3 (without PCM) was more pronounced at lower air velocities. At lower air velocities, a larger portion of the input heat was absorbed by the PCM rather than being transferred to the air in the flow channel through forced convection.

A detailed inspection of the temperature profile T_3 (with PCM) revealed an initial linear increase from $t = 0$ until the onset of PCM melting around the fin jacket within the PCM, marked as point A in Figure 6. This initial heat absorption was characterized by the PCM's sensible heat, associated with its heat capacity and thermal conduction. The onset of PCM melting occurred when the temperature T_3 reached approximately 38 °C, leading to a reduced rate of temperature increase as the PCM began to absorb heat primarily in the form of latent heat, which was significantly higher than its sensible heat. For example, with an air velocity of $V_{\text{air}} = 2 \text{ m/s}$, the onset of PCM melting began at about $t = 15 \text{ min}$ and lasted

for approximately 6 min, during which the PCM adjacent to the fin jacket transitioned from solid to mushy and eventually to liquid phase (the region enclosed by the red dashed oval in Figure 6, corresponding to a high heat absorption period). The temperature increase in T_3 (with PCM) slowed down until point B ($t \approx 48$ min for $V_{\text{air}} = 2$ m/s). The melting process in segment AB was governed by mixed conduction and natural convection within the molten PCM, resulting in relatively constant heat absorption.

In segment BC, natural convection within the molten PCM surrounding the fin jacket accelerated, enhancing the heat transfer rate from the fin jacket to the PCM and causing a second decline in the temperature rise, shown as the region encircled by the black dashed oval in Figure 6 ($t \approx 78$ min for $V_{\text{air}} = 2$ m/s at point C). At some point during segment BC, all the molten PCM around the three fin jackets became interconnected. Beyond point C, the PCM reservoir was predominantly occupied by molten PCM, and the subsequent temperature increase in T_3 (with PCM) was primarily due to the absorption of sensible heat rather than latent heat, corresponding to a period of decreasing heat absorption.

Despite the setup being well-insulated to minimize thermal losses to the environment, an energy balance was conducted between the input and output heat using measured data from various locations on the setup. This involved applying conduction analysis through the thickness of the 3D-printed parts and the aerogel insulation pad on the battery module and PCM reservoir, as well as convection analysis on the flow channel side. For a total power of $P_t = 16$ W, it was determined that heat loss constituted approximately 4–6% of P_t at air velocities ranging from 4 m/s to 2 m/s.

5.1.3. Cyclic Mode

Experimental results indicate that the PCM effectively reduces and regulates the battery temperature primarily through latent heat absorption during its melting phase. This phenomenon is particularly advantageous when the PCM is subjected to fluctuating thermal loads. Fluctuating thermal loads are commonly encountered in electric vehicles when the batteries experience repeated charging and discharging cycles. To study the performance of the developed BTM under cyclic thermal load, an experiment was run for a cyclic power condition with a maximum total power of 16 W and an air velocity of 2 m/s. The heaters ($P_t = 16$ W) were turned on for 10 min and turned off for the following 5 min, and the cyclic power condition was repeated. The cyclic periods were consistent with the electric car cyclic mode operation presented in [28]. Figure 7 shows the battery temperature under the cyclic condition. As shown in this figure, the PCM damped the battery temperature fluctuations compared to those without the PCM. Temperature T_3 in this figure shows that the PCM experienced both melting and solidification as T_3 moved to about 38 °C. During the melting process, the PCM absorbs thermal energy, while during solidification, it releases stored heat.

A comparison between Figures 6b and 7 demonstrates an additional advantage of incorporating PCM in the design, particularly during cyclic operations. As shown in Figure 6b, the battery temperature surpasses 50 °C after approximately 38 min, whereas in Figure 7, it remains below 50 °C for up to 2 h and is expected to stay below 50 °C until the average battery temperature stabilizes at a steady-state condition, as nearly depicted in Figure 7. The average battery temperature in the steady-state condition for cyclic operation is around 45 °C in Figure 7. This indicates that, for the same air velocity, the PCM configuration can potentially accommodate relatively higher fluctuating thermal loads in cyclic operation, keeping the battery temperature below 50 °C for a longer duration compared to non-cyclic operation.

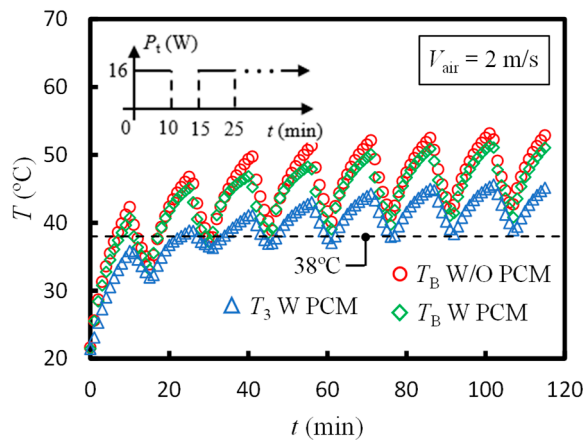


Figure 7. Battery temperature in cyclic operation at an air velocity of 2 m/s, with and without the PCM.

The battery temperature in a non-cyclic input power operation represents an extreme case of cyclic input power operation, where the power time ratio (defined as the duration when the power is on to the duration when the power is off, such as 10 min/5 min in Figure 7) approaches infinity. For any power time ratio between 0 and infinity during cyclic operation, the average battery temperature is expected to be lower than in non-cyclic operation for the same power and air velocities. This demonstrates the robustness and applicability of the cooling system incorporating PCM under varying operational conditions.

5.2. Numerical Results

Numerical simulations were conducted to complement the experimental results and provide deeper insight into the physics of the problem, which are explained here. The heat transfer coefficients on the air-cooled section of the HPs were determined numerically using the computational domain shown in Figure 4a. Air entered the test section at uniform velocities ranging from 2 to 4 m/s, and a boundary layer began to develop along the walls. However, the distance from the inlet to the HPs was shorter than the length required for the boundary layer to transition into a turbulent regime, ensuring that the airflow over the HPs remained laminar. Additionally, the Richardson number was calculated to be approximately 0.003 at the lowest airspeed, indicating that the flow was sufficiently fast to suppress the effects of natural convection at the given velocity. A constant power of 8 W (corresponding to a total power, P_t , of 16 W) was applied at the outer surface of the heat sink in contact with the aluminum housing. Once steady-state conditions were achieved, the average heat flux and temperature at the finned and unfinned surfaces of the HPs exposed to the airflow were calculated. The heat flux was subsequently divided by the temperature difference between the exposed surface and the inlet air to calculate the average heat transfer coefficient. Convective heat transfer coefficients of 38, 51, and 64 W/m²·K were obtained for inlet air velocities of 2, 3, and 4 m/s, respectively. The convective heat transfer coefficients were found to be nearly linear within the range of velocities studied. The simulation was not conducted for the case where $V_{\text{air}} = 0$, which corresponds to natural convection, as the time required for the battery to reach 50 °C is relatively short compared to the forced convection cases and is not of practical interest. The following Fluent settings outlined in Table 2 were employed in the integrated HP-fin-PCM model:

Table 2. Settings used in the integrated HP-fin-PCM BTM model implemented in ANSYS Fluent.

Velocity-pressure coupling algorithm	SIMPLE
Gradient spatial discretization scheme	Least squares cell based
Pressure spatial discretization scheme	PRESTO!
Density spatial discretization scheme	QUICK
Momentum spatial discretization scheme	QUICK
Energy spatial discretization scheme	QUICK
Transient formulation	First order implicit
Mesh size (Number of control volumes)	1,350,000
Under relaxation factors	Pressure: 0.5 Density: 1 Momentum: 0.5 Liquid fraction: 1 Energy: 1
Residuals	Continuity: 10^{-4} velocity: 10^{-4} Energy: 10^{-9}
Mushy zone constant	10^5
Time step size	0.5 s

5.2.1. Comparison of Numerical Predictions with Experimental Data

The numerical predictions of battery temperatures were validated against experimental results, as illustrated in Figure 8, for a total input power of 16 W and varying air velocities. The predicted battery temperatures exhibited behavior consistent with experimental measurements. The agreement between the predicted values and the measurements was within an acceptable range. The discrepancies observed between the predicted values and experimental data were attributed to uncertainties in the PCM properties and differences between the computationally determined convective heat transfer coefficients and the actual values, as well as the assumptions made in the model.

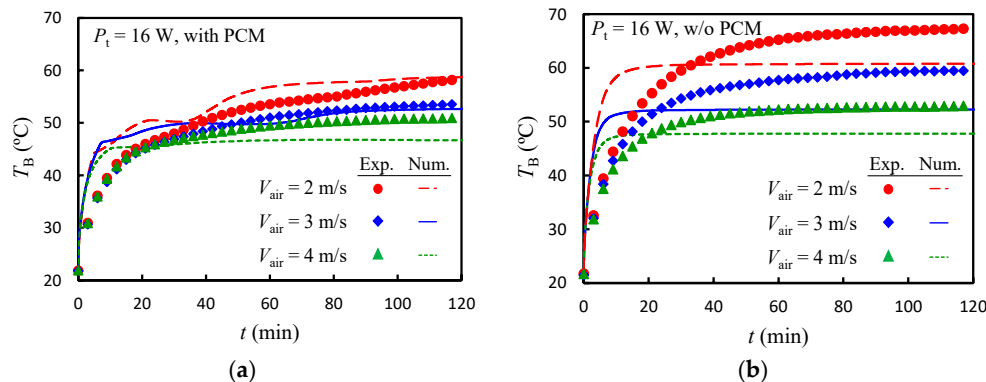


Figure 8. Comparison of predicted and measured battery temperatures for a total input power of 16 W at different air velocities: (a) with PCM; (b) without PCM.

As can be observed in Figure 8, at $t = 120$ min the computational results underpredicted the battery temperature. This underprediction is quantified by dividing the difference between the experimental and numerical battery temperatures by the experimentally measured temperature rise of the battery relative to its initial temperature. For cases with (without) PCM at $t = 120$ min, the numerical results underpredicted the experimental measurements by -1% (20%), 12% (24%), and 20% (22%) for air velocities of 2, 3, and 4 m/s, respectively. At earlier times, the computational results overpredicted the mea-

sured temperatures. This discrepancy was primarily attributed to the thermal mass of the acrylic walls, insulation, and the heater element, which were not accounted for in the computational model.

5.2.2. Heat Absorption Predictions by the PCM

Figure 9 shows the computationally predicted evolution of the PCM melt fraction and the normalized power (heat transfer) to the PCM for air velocities of 2 m/s and 4 m/s, with a total power P_t of 16 W. The heat transfer to the PCM is normalized by dividing it by the heat input from the battery ($P_t = 16$ W). As evident, the heat transfer to the PCM was greater when the air velocity was smaller. This was attributed to the reduced convective heat transfer to the air, which resulted in a higher amount of heat being absorbed by the PCM. For both cases, the heat transfer to the PCM initially increased and then followed a generally decreasing trend. The initial increase was attributed to the rapid rise in the HP temperature. When the PCM temperature reached the melting temperature, melting commenced, and the melt layer thickness continuously increased, corresponding to an increasing thermal resistance. On the other hand, the thermal resistance between the finned surface of the HPs and air remained constant. As such, the heat transfer to the PCM slowly decreased during melting. Once the melting process was complete, the PCM's heat absorption diminished rapidly, as observed for an air velocity of 2 m/s.

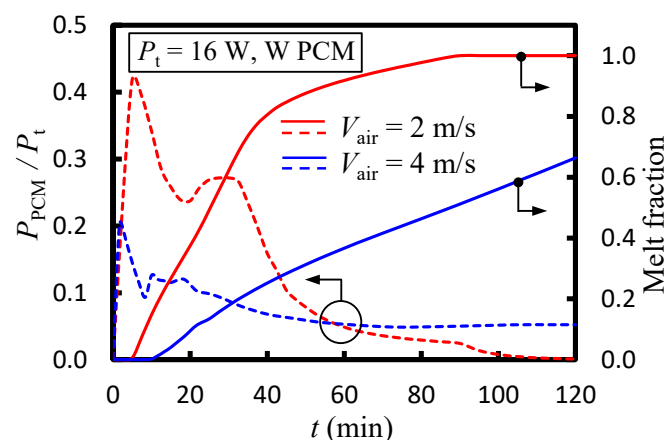


Figure 9. Computationally determined time variations of the melt fraction (solid lines) and normalized heat transfer to the PCM (dashed lines) for air velocities of 2 m/s and 4 m/s, with $P_t = 16$ W.

Regarding the PCM melt fraction, as shown in Figure 9, increasing the air velocity decreased the melting rate due to more effective convective heat transfer to the air, which reduced the heat transfer to the PCM and slowed down the melting process.

5.2.3. Representative Contours of Temperature

Figure 10 illustrates the temperature contours on the symmetry plane of the computational domain (x - z plane, as shown in Figure 4b) at 15 min intervals for a total power input of 16 W and an air velocity of 2 m/s. This figure illustrates the temporal evolution of natural convection within the molten PCM over time, as well as the nearly isothermal nature of the HPs throughout the entire duration of the experiment. As anticipated, the lowest temperatures were observed at the bottom of the PCM reservoir, while the highest temperatures occurred at the aluminum heat sink.

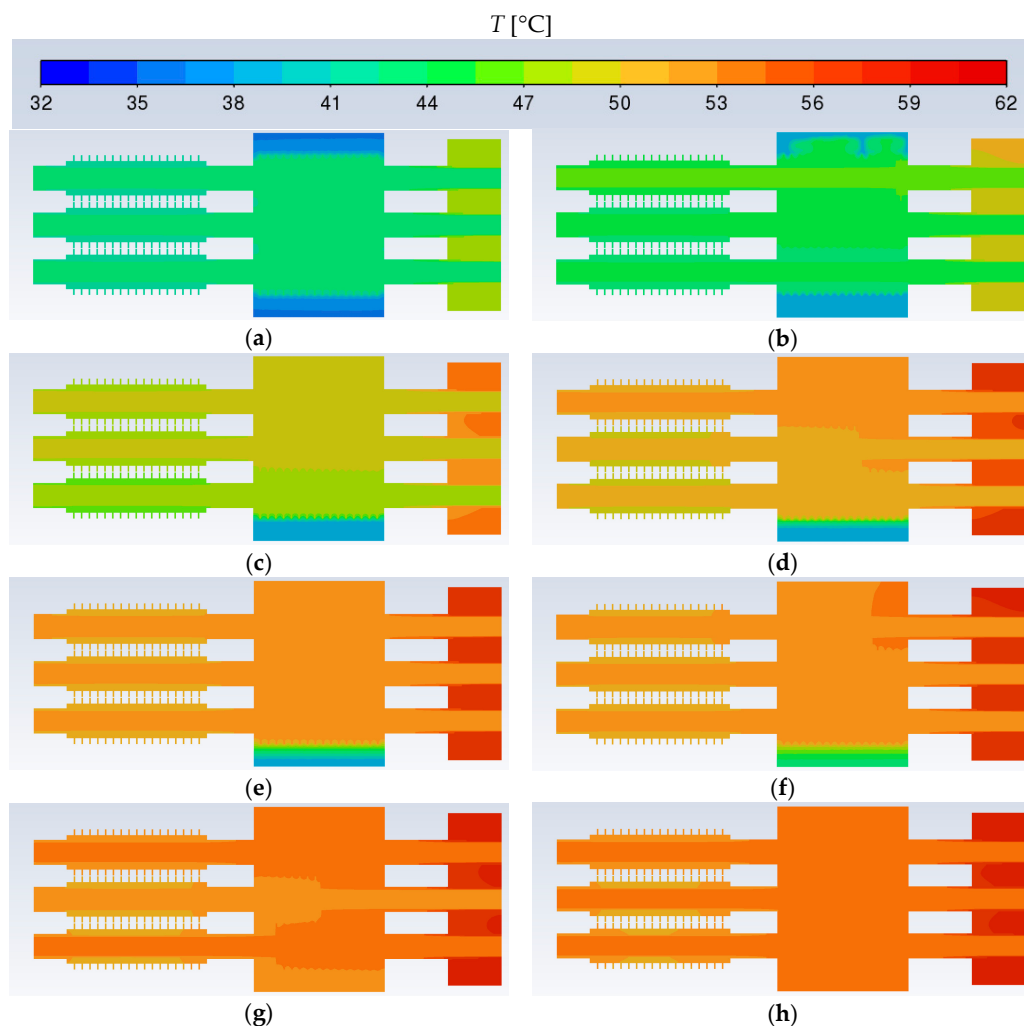


Figure 10. Temperature contours on the symmetry plane (x-z plane in Figure 4b) at 15-min intervals for a total power of 16 W and an air velocity of 2 m/s: (a) $t = 15$ min, (b) $t = 30$ min, (c) $t = 45$ min, (d) $t = 60$ min, (e) $t = 75$ min, (f) $t = 90$ min, (g) $t = 105$ min, (h) $t = 120$ min.

The temperature contours within the PCM reservoir, depicted in Figure 10b, reveal that natural convection within the molten PCM intensified as the warm molten PCM migrated toward the top of the PCM reservoir. Consequently, the lower portion of the PCM remained relatively cooler compared to the upper region. Examination of the temperature distribution in the lower PCM reveals a gradual warming trend toward its melting temperature over time, eventually reaching this state after around 90 min, as shown in Figure 10f. This observation aligns with the experimental results presented in Figure 6, particularly with the discussion regarding the temperature comparison between T_5 and T_6 .

After about 90 min, the entire PCM transitioned to a liquid phase, as evidenced by Figure 10g,h. The HP cores (vapor space) exhibit a uniform temperature distribution throughout at each time interval shown in Figure 10, highlighting the near-isothermal behavior of the HPs and their efficiency in transferring heat.

To further analyze and investigate the internal heat transfer mechanisms of the HP, particularly the interaction between the HP and PCM, the heat flux distribution at the wick-vapor interface of the middle HP was examined at representative time intervals: $t = 1$ min, during the initial stages; $t = 30$ min, when natural convection within the molten PCM was accelerating; and $t = 120$ min, when the system was approaching thermal equilibrium. The heat flux distributions for these time intervals are presented in Figure 11.

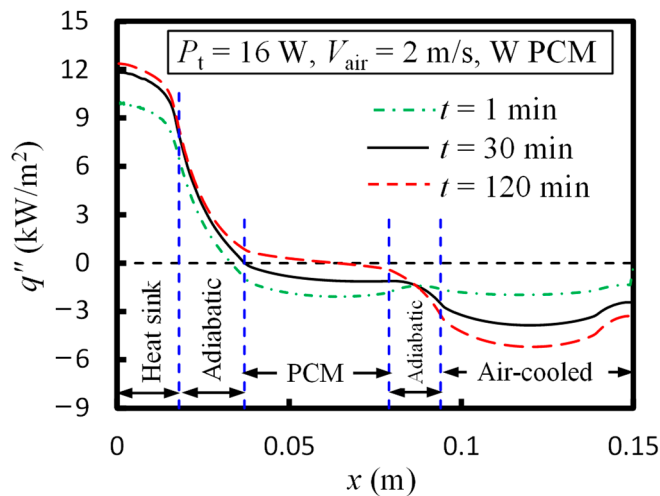


Figure 11. Heat flux distribution at the wick-vapor interface of the middle HP at $t = 1$, $t = 30$ and 120 min for a cooling air velocity of 2 m/s and a total power of 16 W .

In the figure, regions with positive heat flux correspond to evaporation zones within the HP, where heat is transferred into the HP, while regions with negative heat flux indicate condensation zones, where heat is released from the HP. As time progressed, the highest heat flux was observed in the heat sink section of the HP, where heat is absorbed, while the lowest heat flux was seen in the air-cooled section, where heat is dissipated to the ambient air.

A notable heat transfer phenomenon was observed within the PCM section. At the early stage ($t = 1 \text{ min}$), the PCM absorbed heat from the HP at its highest rate, as indicated by the relatively large negative heat flux. This occurred because the HP was significantly warmer than the PCM. By $t = 30 \text{ min}$, at the intermediate stage, heat absorption from the HP continued, but at a reduced rate. Finally, at $t = 120 \text{ min}$, as the system neared thermal equilibrium, the PCM simultaneously absorbed and released heat to the HP at its lowest rate. This is indicated by the coexistence of positive and negative heat flux regions within the PCM section.

In the air-cooled section of the HP, the magnitude of localized heat flux decreased toward the tip of the HP compared to its midsection. This decrease was attributed to the portion of the HP within the flow channel that was not covered by the fin jacket (approximately 10.55 mm). Overall, these findings highlight the complex heat transfer dynamics within the HP-fin-PCM system and the effectiveness of the numerical model in capturing these phenomena.

More detailed predictions, including contours of PCM melt fraction and velocity fields, are provided in Appendix A for further reference.

6. Conclusions

An experimental and numerical investigation was carried out on a new setup comprising heat pipes, fins, and PCM to evaluate the thermal performance of a hybrid cooling method for lithium-ion battery thermal management. Unlike recent studies, where the PCM is typically in direct contact with the batteries, this design innovatively decouples the PCM from the batteries and positions it between the batteries and the air-cooled section. This decoupling not only reduces the complexity of the system but also enhances design flexibility and facilitates easier battery maintenance or replacement.

The study encompassed various operating conditions, including different input powers, air velocities, and operating modes (with and without PCM, and cyclic mode). In general, incorporating PCM led to a decrease in the battery surface temperature when

compared to scenarios without PCM. Specifically, for a total input power of 16W, steady-state battery temperatures were reduced by approximately 14%, 10%, and 4% with PCM compared to without PCM for air velocities of 2 m/s, 3 m/s, and 4 m/s, respectively. The battery temperature was maintained at about and below 50 °C for cooling air velocities of 3 m/s and 4 m/s. The advantages of PCM were observed to be more significant at lower air velocities and in cyclic battery operation. The predictions exhibited satisfactory agreement with the experimental data, validating the numerical model's effectiveness in accurately simulating the underlying physics. The proposed model provides a robust foundation for future optimization studies. The new HP-fin-PCM design emerges as a promising candidate for BTM systems in electric vehicles. While this study focused on a single module of the HP-fin-PCM system, future research should extend this investigation to multiple modules within a battery pack. Such studies could reveal the full extent of the benefits offered by the HP-fin-PCM configuration. Additional investigations are needed to explore the effects of various PCMs with different melting temperatures, air inlet temperatures, the impact of the number of fins, and the use of smart fans on the battery surface temperature.

Author Contributions: Conceptualization and methodology, N.S. and H.S.; SolidWorks Design and construction, C.M., U.E. and N.S.; data collection, N.S.; numerical simulations, H.S.; writing, N.S. and H.S.; proof read, C.M. and U.E.; supervision, N.S.; project administration, N.S.; funding acquisition, N.S. All authors have read and agreed to the published version of the manuscript.

Funding: This research was funded by Tarleton State University President's Excellence in Research Scholars (PERS) grant and Mayfield College of Engineering.

Data Availability Statement: Data are available on request.

Acknowledgments: This study was supported by the Tarleton State University President's Excellence in Research Scholars (PERS) grant and Mayfield College of Engineering. The faculty also wish to thank undergraduate students Christian Millard, Ugochukwu Etufugh, and Griffin DaRosa for their assistance in constructing the experimental setup.

Conflicts of Interest: The authors declare no conflicts of interest.

Nomenclature

A	mushy-zone constant function
A_{mushy}	mushy-zone constant
BTM	battery thermal management
CNC	computer numerical control
c_p, C_p	specific heat (J/kg K or J/kg °C)
EV	electric vehicle
g	gravitational acceleration (m/s ²)
h, H	enthalpy (J/kg)
h_{fg}	latent heat of vaporization of the HP working fluid (kJ/kg)
h_{sl}	latent heat of fusion of the PCM (kJ/kg)
HP	heat pipe
ID	inner diameter (m or mm)
k	thermal conductivity (W/m·K)
L	length (m or mm)
L_f	latent heat of fusion (kJ/kg)
\dot{m}''	mass flux (kg/m ² s)
OD	outer diameter (m or mm)
P	pressure (Pa)
PLA	polylactic acid (3D printer filament material)
PCM	phase change material

P_B	individual battery power (W) or individual heater power (W)
P_{PCM}	heat transfer or power to the PCM (W)
P_t	total heater power (W); $P_t = 2P_B$
q''	heat flux (W/m^2 or kW/m^2)
R_g	gas constant ($\text{J}/\text{kg K}$)
S_m	source term (N/m^3)
t	time (s or min)
T	temperature (K or $^\circ\text{C}$)
T_{air}	air temperature (K or $^\circ\text{C}$)
TC	thermocouple
T_m	melting temperature (K or $^\circ\text{C}$)
V	velocity vector (m/s)
V^T	transposed velocity vector (m/s)
x, y, z	coordinates (m or mm)
<i>Greek</i>	
ΔT	half width of temperature range (K)
β	thermal expansion coefficient (1/K)
ε	small value
λ	liquid fraction
μ	viscosity (Pa.s)
ρ	density (kg/m^3)
<i>Subscript</i>	
B	battery
l	liquid
ref	reference
s	solid
sat	saturation
v	vapor
w	wall

Appendix A

The following figures provide additional insights into the thermal and fluid dynamics observed during the simulation. These figures aim to complement the main results by illustrating specific phenomena in greater detail.

Figure A1 shows the PCM melt fraction and z-velocity vectors on the y - z plane crossing through the middle of the PCM reservoir at $t = 25$ min, when natural convection is in the process of accelerating. The melted region is relatively greater around the top HP due to the influence of natural convection, which drives the warmer PCM upward. Accumulation of warmer PCM at the upper region creates more melting relative to the lower region as depicted in Figure A1a. Within the melted region, the liquid PCM near the HPs is relatively warmer and moves upward due to relatively lower density. Near the interface with the solid PCM, the liquid PCM is relatively colder and descends due to higher density as seen in Figure A1b.

Figure A2 shows the axial water vapor velocity contours within the HPs vapor spaces at time intervals: $t = 1$ min, during the initial stages; $t = 30$ min, when natural convection within the molten PCM is accelerating; and $t = 120$ min, when the system approaches thermal equilibrium. The right end is in contact with the aluminum heat sink, which serves as the heating section. To enhance clarity and avoid visual clutter, the vapor velocity vectors are displayed for only one HP, providing a clearer representation of the flow direction during acceleration and deceleration. As evident, the maximum vapor velocities occur somewhere between the heating section and the PCM reservoir. In this region, thermal

energy enters the HPs and evaporates the HPs working fluid. The vapor flows toward the relatively colder sections of the HP, while more vapor is added to the vapor space due to ongoing evaporation. When the vapor reaches the cooled sections of the HPs, condensation removes mass from the vapor space, resulting in decreasing axial velocity. It is observed that the vapor velocities decrease as time increases. The smaller velocities are attributed to the greater vapor temperatures, which correspondingly create greater pressures at later times due to the coupled relationship between vapor temperature and pressure under saturation conditions (see Figure 10). As the vapor pressure increases, its density increases and the same amount of heat can be transported by a smaller vapor volumetric flowrate. The average absolute vapor pressures at $t = 1, 30$, and 120 min were about 3.6 kPa, 9.5 kPa and 14.4 kPa, respectively. Meanwhile, the average vapor densities were 0.026 kg/m³, 0.065 kg/m³ and 0.096 kg/m³, for $t = 1, 30$, and 120 min, respectively.

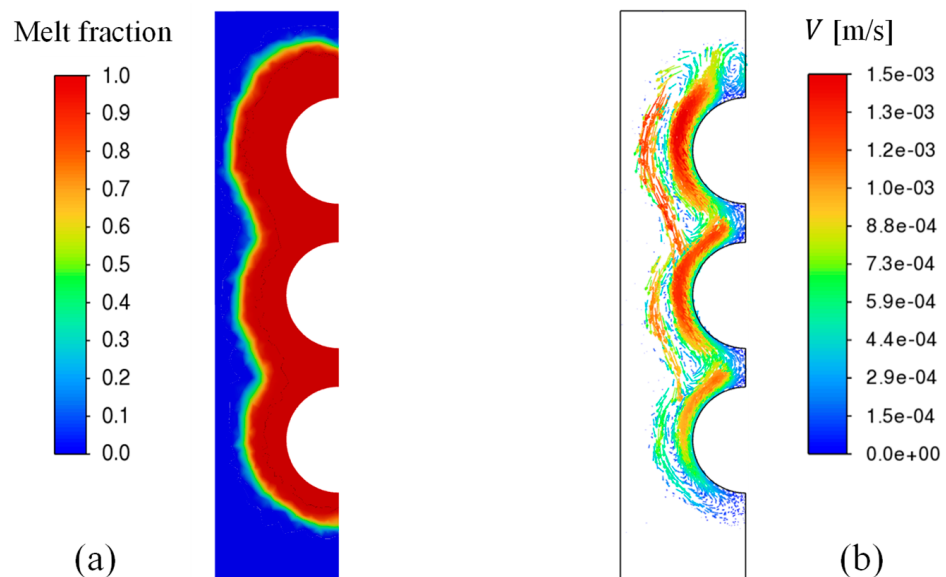


Figure A1. (a) PCM melt fraction, and (b) z-velocity -vectors on y-z plane crossing through the middle of the PCM reservoir at time $t = 25$ min, with a cooling air velocity of 2 m/s and a total power of 16 W.

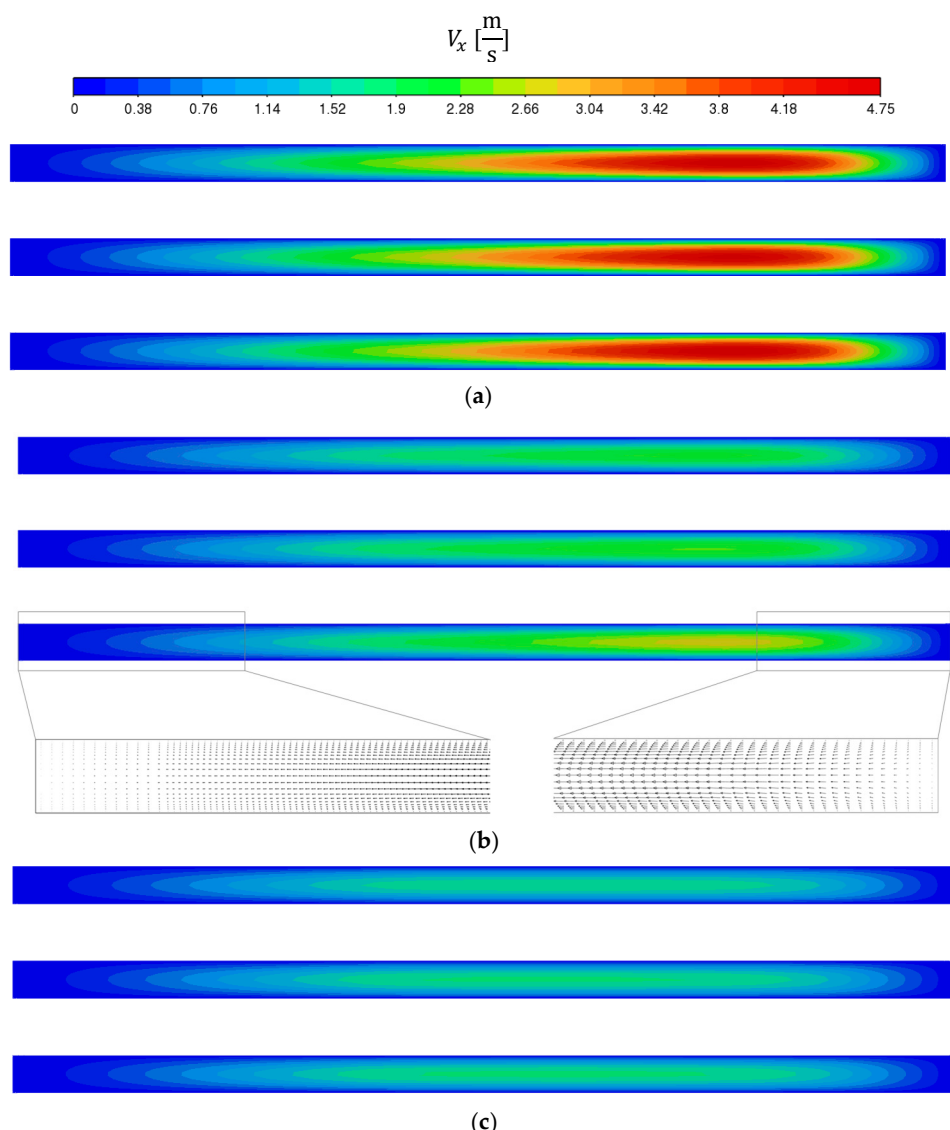


Figure A2. Axial vapor velocity contours within the HPs for a cooling air velocity of 2 m/s and a total power of 16 W: (a) $t = 1$ min; (b) $t = 30$ min; (c) $t = 120$ min (the right end is in contact with the hot aluminum heat sink).

References

- Ma, S.; Jiang, M.; Tao, P.; Song, C.; Wu, J.; Wang, J.; Deng, T.; Shang, W. Temperature effect and thermal impact in lithium-ion batteries: A review. *Prog. Nat. Sci. Mater. Int.* **2018**, *28*, 653–666. [[CrossRef](#)]
- Rahmani, A.; Dibaj, M.; Akrami, M. Recent Advancements in battery thermal management systems for enhanced performance of Li-Ion batteries: A comprehensive review. *Batteries* **2024**, *10*, 265. [[CrossRef](#)]
- Ahmadian-Elmi, M.; Zhao, P. Review of thermal management strategies for cylindrical lithium-ion battery packs. *Batteries* **2024**, *10*, 50. [[CrossRef](#)]
- Weragoda, D.M.; Tian, G.; Burkittbayev, A.; Lo, K.H.; Zhang, T. A comprehensive review on heat pipe based battery thermal management systems. *Appl. Therm. Eng.* **2023**, *224*, 120070. [[CrossRef](#)]
- Bernagozzi, M.; Georgoulas, A.; Miché, N.; Marengo, M. Heat pipes in battery thermal management systems for electric vehicles: A critical review. *Appl. Therm. Eng.* **2023**, *219*, 119495. [[CrossRef](#)]
- Faghri, A.; Zhang, Y. *Transport Phenomena in Multiphase Systems*; Academic Press, Elsevier: New York, NY, USA, 2006.
- Faghri, A. *Heat Pipe Science and Technology*, 2nd ed.; Global Digital Press, 2016.
- Sharifi, N.; Bergman, T.L.; Allen, M.J.; Faghri, A. Melting and solidification enhancement using a combined heat pipe, foil approach. *Int. J. Heat Mass Transf.* **2014**, *78*, 930–941. [[CrossRef](#)]
- Shabgard, H.; Faghri, A.; Bergman, T.L.; Andraka, C.E. Numerical simulation of heat pipe-assisted latent heat thermal energy storage unit for dish-stirling systems. *J. Sol. Energy Eng.* **2014**, *136*, 021025. [[CrossRef](#)]

10. Sharifi, N.; Roesler, D.; Gold, A.; Shabgard, H. Thermal management system for lithium-ion batteries using phase change material, heat pipes and fins. *ASME Int. Mech. Eng. Congr. Expo.* **2023**, 87677, V010T11A049.
11. Zhang, C.; Yu, M.; Fan, Y.; Zhang, X.; Zhao, Y.; Qiu, L. Numerical study on heat transfer enhancement of PCM using three combined methods based on heat pipe. *Energy* **2020**, 195, 116809. [[CrossRef](#)]
12. Gao, C.; Sun, K.; Song, K.; Zhang, K.; Hou, Q. Performance improvement of a thermal management system for Lithium-ion power battery pack by the combination of phase change material and heat pipe. *J. Energy Storage* **2024**, 82, 110512. [[CrossRef](#)]
13. Sutheesh, P.M.; Nichit, R.B.; Rohinkumar, B. Numerical investigation of thermal management of lithium ion battery pack with nano-enhanced phase change material and heat pipe. *J. Energy Storage* **2024**, 77, 109972. [[CrossRef](#)]
14. Sharma, D.K.; Agarwal, P.; Prabhakar, A. Effect of fin design and continuous cycling on thermal performance of PCM-HP hybrid BTMS for high ambient temperature applications. *J. Energy Storage* **2023**, 74, 109360. [[CrossRef](#)]
15. Tang, Z.; Feng, R.; Huang, P.; Bai, Z.; Wang, Q. Modeling analysis on the cooling efficiency of composite phase change material-heat pipe coupling system in battery pack. *J. Loss Prev. Process Ind.* **2022**, 78, 104829. [[CrossRef](#)]
16. Abbas, S.; Ramadan, Z.; Park, C.W. Thermal performance analysis of compact-type simulative battery module with paraffin as phase-change material and flat plate heat pipe. *Int. J. Heat Mass Transf.* **2021**, 173, 121269. [[CrossRef](#)]
17. 1-tetradecanol: 112-72-1. ChemicalBook. Available online: https://www.chemicalbook.com/ChemicalProductProperty_EN_CB8689436.htm (accessed on 3 January 2025).
18. Jiang, Z.Y.; Qu, Z.G. Lithium-ion battery thermal management using heat pipe and phase change material during discharge-charge cycle: A comprehensive numerical study. *Appl. Energy* **2019**, 242, 378–392. [[CrossRef](#)]
19. Available online: <https://us.amazon.com/Aerogel-Insulation-Padding-Manufacturing-Lightweight/dp/B0BWV9ZSK> (accessed on 3 January 2025).
20. Akula, R.; Minnikanti, A.; Balaji, C. Pin fin-PCM composite heat sink solution for thermal management of cylindrical Li-ion battery. *Appl. Therm. Eng.* **2024**, 248, 123146. [[CrossRef](#)]
21. Available online: <https://www.graspengineering.com/material-properties-aluminum-6061-t6-6061-t651/> (accessed on 3 January 2025).
22. Mishra, G.; Memon, A.; Gupta, A.K.; Nirmalkar, N. Computational study on effect of enclosure shapes on melting characteristics of phase change material around a heated cylinder. *Case Stud. Therm. Eng.* **2022**, 34, 102032. [[CrossRef](#)]
23. Mahdavi, M.; Faghri, A.; Shabgard, H. Thermal performance of U-shaped and L-shaped heat pipes. *Numer. Heat Transf. Part A Appl.* **2021**, 80, 411–435. [[CrossRef](#)]
24. Calle-Arroyo, C.; Lopez-Fidalgo, J.; Rodríguez-Aragon, L.J. Optimal designs for Antoine Equation. *Chemom. Intell. Lab. Syst.* **2021**, 214, 10433. [[CrossRef](#)]
25. Cao, Y.; Faghri, A. Transient two-dimensional compressible analysis for high temperature heat pipes with pulsed heat input. *Numer. Heat Transf. Part A Appl.* **1990**, 18, 483–502. [[CrossRef](#)]
26. Voller, V.R.; Prakash, C. A fixed grid numerical modelling methodology for convection-diffusion mushy region phase-change problems. *Int. J. Heat Mass Transf.* **1987**, 30, 1709–1719. [[CrossRef](#)]
27. Zhuang, W.; Liu, Z.; Su, H.; Chen, G. An intelligent thermal management system for optimized lithium-ion battery pack. *Appl. Therm. Eng.* **2021**, 189, 116767. [[CrossRef](#)]
28. Liu, H.; Chen, F.; Tong, Y.; Wang, Z.; Yu, X.; Huang, R. Impacts of driving conditions on EV battery pack life cycle. *World Electr. Veh. J.* **2020**, 11, 17. [[CrossRef](#)]

Disclaimer/Publisher’s Note: The statements, opinions and data contained in all publications are solely those of the individual author(s) and contributor(s) and not of MDPI and/or the editor(s). MDPI and/or the editor(s) disclaim responsibility for any injury to people or property resulting from any ideas, methods, instructions or products referred to in the content.